Article:
Qi, J. orcid.org/0000-0001-5235-0027, Bai, M., Nutter, J. et al. (2 more authors) (2025) Correlation of micromechanical property and microstructure of tribo-layers. Wear. 205785. ISSN 0043-1648

https://doi.org/10.1016/j.wear.2025.205785

Wear xxx (xxxx) xxx

Contents lists available at ScienceDirect

Wear

journal homepage: www.elsevier.com/locate/wear

Correlation of micromechanical property and microstructure of tribo-layers

J. Qi, M. Bai, J. Nutter, B. Inkson, W.M. Rainforth *

Department of Material Science and Engineering, The University of Sheffield, Sheffield, S1 3JD, UK

ARTICLE INFO

Keywords:
Ti-6Al-4V
Tribocorrosion
Micromechanical properties

ABSTRACT

Tribological contact often leads to surface deformation, resulting in a substantial increase in dislocation density and a considerable refinement in the microstructural scale. The extensive work hardening associated with this results in significant changes in the mechanical properties of the surface. It is not only the mechanical properties that change, but also the corrosion potential. In some cases, the surface changes enhance the wear resistance of the material. However, in other cases, higher wear rates are found with surface deformation that results in ultra-fine surface structures. Despite the importance of surface deformation, much is unknown about the mechanical properties of the wear induced surface layers. Nanoindentation provides useful information but does not give a good indicator of the ductility. The challenge is to test the mechanical properties of such a fine scale deformed structure. In this work, the micromechanical properties of Ti-6Al-4V worn surfaces after tribocorrosion testing were measured using an in-situ micropillar compression method in the chamber of a scanning electron microscope. Reciprocating tribocorrosion testing was undertaken in 25 vol % Bovine Serum Albumin (BSA) in phosphate-buffered saline (PBS) solution against an alumina counterface, with a load of 0.5N and a speed of 20 mm/s. Tests were conducted under Open Circuit Potential (OCP) conditions and at cathodic and anodic surface potentials, namely at +0.5V and −0.95V. The different test conditions resulted in different extents of surface deformation. This resulted in significant differences in the stress strain curves from the micropillar tests, both in terms of strength and ductility. The microstructure observed by subsequent TEM of the tested micropillars is correlated with the mechanical properties and the reasons for the different mechanical properties are discussed.

1. Introduction

Tribocorrosion plays an important role in implant degradation in the human body where two metal components are in frictional contact, or a metal component is in contact with another surface such as a bone or a ceramic or cement component. There are three interrelated components to tribocorrosion: tribology (friction, wear and lubrication), corrosion (the material and its environment) and biochemistry (interaction between cells and protein and the surface) [1,2]. Key to all of these is the manner in which the material surface behaves in response to the chemical and mechanical environment.

The dynamic microstructural changes induced by tribological contacts can determine the wear resistance of a material. It is well known that frictional contact results in microstructural changes at the surface that change the mechanical properties. Changes can arise from the plastic deformation, but also significant changes arise from electrochemical effects. Thus, it is vital to understand how the surface microstructure changes, and how this modifies the surface mechanical properties and chemical activity [3].

Tribological contact inevitably alters the dislocation density, grain orientation and grain size of the surface [4]. These changes will affect all the key mechanical properties such as the yield strength, strain hardening coefficient, ductility, hardness and toughness. Therefore, measuring the dislocation density, grain orientation and grain size is key to understanding the surface mechanical properties. There have been many attempts to measure these variables using electron backscatter diffraction (EBSD) in the SEM, but all have been hampered by the resolution limit, typically no better than 100 nm, and the inability of the technique to give an adequate signal in a heavily deformed structure. Transmission electron microscopy (TEM) offers the required spatial resolution, but it is difficult using conventional imaging and diffraction to build up a statistically meaningful map of the surface regions. A recently introduced superior technique using transmission electron microscopy (TEM) and scanning transmission electron microscopy (STEM)

This article is part of a special issue entitled: WOM2025 published in Wear.

* Corresponding author.
E-mail address: m.rainforth@sheffield.ac.uk (W.M. Rainforth).

https://doi.org/10.1016/j.wear.2025.205785
Received 23 August 2024; Received in revised form 27 November 2024; Accepted 13 December 2024
Available online 2 February 2025

is precession electron diffraction (PED). This offers the ability to quantify phase constitution and crystal orientation with a spatial resolution of ~3–5 nm depending on the material and conditions and can even give spatial resolution down to 0.5 nm. With an angular resolution of ~0.1°, PED has been used to resolve individual dislocations, dislocation dipoles and deformation structures [5]. For example, Liu et al. [6] used PED to obtain the geometrically necessary dislocation (GND) density distribution from a large deformation region to investigate the failure mechanism at adiabatic shear bands of a titanium alloy. Similarly, Ghamarian et al. used PED to quantify and map the deformation structures in ultrafine-grained titanium [7] and to characterize the defect structure of nanostructured non-ferrous structural alloys [5,8]. There has been only limited use of PED to examine the deformation structures below a worn surface. Qi et al. [9] used PED to examine the deformation substructures in Ti-6Al-4V tested under the same conditions as those reported in the current paper and were able to differentiate the extent of slip activity on basal and prismatic planes in the α-phase and separate this from the extent of deformation in the β-phase. Similarly, Qi et al. [10] were able quantify the extent of martensite transformation at the worn surface of CoCrMo alloys (used for hip joint replacements) and to demonstrate how this transformation controlled the surface deformation behaviour. Clearly, there is considerable scope for using PED to understand the deformation mechanisms at worn surfaces and how they contribute to the wear mechanism.

Nanoindentation has been widely used to measure the mechanical properties of a surface, given its ability to generate the reduced and Young's modulus, the yield strength and the hardness [11,12]. Generally, the nanoindentation shows that the frictional contact results in considerable hardening of the surface in a wide range of materials, including CoCrMo, Ti-6Al-4V, Ni, W and so on. This has often led to the view that such heavily worked hardened layers, with greatly increased yield strengths, should exhibit much better wear resistance. But this is often not the case. For example, Perret et al. [13] and Maldonado et al. [14] found that the deformation of the material underneath the rubbed surface depends on the local electrochemical conditions prevailing during tribocorrosion and that testing a 316L stainless steel under anodic conditions, which led to the largest and most refined nanocrystalline layer, coincided with the highest wear rates. Similarly, Namus et al. [12] tested CoCrMo alloys under OCP conditions and showed that the highest wear rates coincided with the thickest nanocrystalline structure. More recently, Namus et al. [15] took a CoCrMo alloy and processed the bulk material it to give a microcrystalline structure and a nanocrystalline structure, which were compared to the conventional microstructure, showing that the mechanical wear rate did not change with grain size across this range from micron to nanocrystalline.

There is an additional issue with nanoindentation experiments. It is often observed that there is an inverse relationship between the hardness and the indentation depth [16–22], the so-called indentation size effect. Unless this relationship is known for a specific material, then it is difficult to interpret the values measured under single test size. This is often ignored in such measurements.

In situ micromechanical property evaluation of tribo-surfaces by micropillar compression has been used as an approach to measure the surface's mechanical properties, seeking to overcome the constraints of nanoindentation (such as measurement scale and the low forces applied). Moreover, nanoindentation requires a flat, well prepared surface, which is not suited to measurements on typical worn surfaces, whereas micropillars are far less sensitive to surface roughness [23]. Battaile et al. [11] conducted nanopillar compression to investigate the mechanical properties of tribofilms on single crystal nickel slid against a hard spherical counter face (Si_3N_4) in dry nitrogen. They demonstrated a contradiction between nanoindentation and micropillar results, with the nanoindentation showing the tribofilm to be about twice as hard as the single crystal Ni, while the micropillars indicated that the tribofilm was twice as soft as the micropillars taken from an unworn surface. They considered that the differences in constraint between the micropillar and nanoindentation explained the significantly different results. Similarly, Stoyanov et al. [24] also observed surface softening in W after sliding against WC in ambient conditions using micropillar testing.

In this paper we report on the use of micropillars to characterize the mechanical properties of worn surfaces where the tribocorrosion behaviour has been comprehensively characterised. The micropillar results are compared to the nanoindentation hardness. The deformed surface structure is comprehensively characterised using TEM and PED allowing an understanding of the observed mechanical properties.

2. Experimental

2.1. Materials

An Extra Low Interstitial grade of a commercial Ti-6Al-4V alloy was obtained as 3 mm sheet from the Ti-shop (UK), with a composition that complies with ASTM F136 for surgical implant applications. The Ti-6Al-4V sheet was sectioned into 22 × 22 mm square coupons and metallographically polished using standard techniques to an 0.25 μm finish using a silica suspension. The surface roughness of these polished samples was measured with stylus profilometry (Diktak, Veeco), showing values consistently under 10 nm Ra. The polished coupons were thoroughly cleaned using deionised water and isopropanol before tribocorrosion testing.

2.2. Tribocorrosion test procedure

The tribocorrosion tests were carried out using a three-electrode tribocorrosion cell on a TriboLab Universal Micro Tribometer (Bruker) integrated with an EasyStat Potentiostat. An Ag/AgCl reference electrode connected by a platinum wire was used as counter electrode (CE), with the Ti-6Al-4V test material connected as the working electrode. Testing was undertaken in a solution of 25 vol % Bovine Serum Albumin (BSA) (First Link Ltd., UK) in a phosphate-buffered saline (PBS) (Sigma - Aldrich) solution, prepared using ultrapure water (Alfa Aesar). The initial pH of the solution was 7.45, which fell to 7.0 at the end of the test.

A ball on disk reciprocating sliding configuration was used which conformed to ASTM G133. Grade 5 high-precision bearing 4 mm diameter Al_2O_3 balls (99.0 %, Oakwase Ltd., UK) were used as the counterface with a surface roughness specified by the manufacturer as 5–20 nm Ra. A normal load of 0.5 N was applied, which corresponds to an initial Hertzian contact pressure of 600 MPa. The stroke length was 2 mm and the maximum sliding speed was 20 mm/s. The latent time (the time between two successive contact events was 0.1 s). A total sliding distance of 3600 m was used, which is well into the steady state condition. The test temperature was 37 ± 1 °C.

The initial testing was undertaken under Open Circuit Potential (OCP) conditions. Based on this result, further tests were undertaken with applied potentials of +0.5V and −0.95V. These potentials were selected based on our previous work on the tribocorrosion behaviour of Ti-6Al-4V [9]. The test materials were allowed to stabilise for 30 min in the test solution before the load and potential was applied and reciprocating sliding commenced. Tests under each condition were repeated at least 3 times. The potential and the coefficient of friction (COF) were measured as a function of sliding distance.

2.3. Analysis and characterisation of worn surface

After the test, all the samples were rinsed in ultrapure water then left to dry. The wear scar profile and wear volume were measured using a Bruker Alicona surface profiler. The specific wear rate K in mm^3/Nm was calculated by the standard formula:

$$K = \frac{V}{dL}$$

where V is the wear volume of material loss in mm^3, L is the normal load in N and d is the total sliding distance in m.

The morphology of the wear scars was observed by Scanning Electron Microscopy (FEI F50 SEM) operating at 1 kV, equipped with an Energy-dispersive X-ray spectroscopy (EDX) system, with the SEM operating at 10 kV.

2.4. Mechanical testing of the worn surface

The hardness of the worn surface and the cross-section of the subsurface underneath the wear track was measured by nanoindentation (Bruker's Hysitron® TI Premier Nanomechanical Test Instrument) using a Berkovich diamond indenter, whose tip-area function had been calibrated. The surface hardness (H) was determined from the obtained load versus displacement curves [25].

The micro-mechanical properties of the worn surfaces were investigated using the micropillar compression method. The micropillars were fabricated using a dual-beam focused ion beam/field emission scanning electron microscope (FIB/FESEM, FEI Helios Nanolab G3) with a Ga^+ ion source operated at 30 kV. The milling process was carried out in three stages using decreasing ion beam currents from 9.3 nA down to 80 pA to produce micropillars with diameter 1 μm and aspect ratios over 3. Micropillars were compressed uniaxially at room temperature by a 10 μm diamond flat punch (Synton, Switzerland) using an *in situ* SEM (FEI, Nova NanoSEM 450) nanoindenter (Alemnis, Switzerland) under displacement control at a rate of 4 nm s^{-1}, corresponding to a strain rate of $\sim 1 \times 10^{-3}$ s^{-1}. At least 3 micropillars were tested for each tribo-corrosion test condition. The location of the micropillar was chosen based on SEM images of the worn surface, selecting a region that was representative, but also reasonably flat and free from loosely adhered wear debris.

2.5. Characterisation of the worn surface microstructure

Cross-sections of the worn surface were obtained using the FIB (FEI Helios Nanolab G3) lift out procedure. The structure and chemical composition were examined using a cold field emission (c-FEG) JEOL F200 TEM coupled with a twin, solid state, ultra-sensitive large silicon drift detectors (SDD) EDX system operating at 200 kV.

Crystal orientation and deformation substructure were quantified using precession electron diffraction (NanoMegas STAR™ PET and ASTAR™ ACOM-TEM systems) integrated in the JEOL F200 TEM. A precession angle of 1.4° was used, with a precession frequency of 100 Hz and beam spot size of 2 nm. The step size was 7 nm for both x and y directions. Diffraction patterns were collected at a camera length of 150 nm, and the dataset was then matched against simulated diffraction patterns and indexed automatically by Index software (NanoMegas, Belgium). This data was then exported and post-processed using customized MATLAB scripts (originally from MTEX [14]) to calculate the geometrically necessary dislocation (GND) density.

3. Results

3.1. Summary of wear rates and friction coefficients

The friction and wear behaviour have been reported in detail in a previous publication [9]. Fig. 1 shows the variation in the COF and OCP over time under different conditions. Fig. 1A shows the COF and potential evolution under OCP conditions. Fig. 1B and C presents the COF evolution over time under applied potentials of +0.5V and −0.95V and a summary of the specific wear rates for each test condition. The anodic condition of +0.5V resulted in the lowest wear rate, while the cathodic condition of −0.95V resulted in the highest wear rate, with the cathodic condition of −0.95V giving nearly 3x the specific wear rate of the anodic condition.

The friction coefficient values were similar for all conditions, starting at approximately 0.35, gradually reducing to ~0.3 at the end of the test. However, the friction measured under the anodic condition exhibited numerous sharp increases followed by a rapid decrease, associated with the loss of passivation and subsequent repassivation of the surface. The OCP condition gave similar friction behaviour to the anodic condition, except that the depassivation and repassivation events were more numerous. In contrast, friction for the cathodic condition was very noisy, fluctuating between 0.3 and 0.4 early in the test.

Fig. 2 gives representative SEM images of the worn surface. The wear scar was dominated by classic ploughing giving a heavily grooved surface. At +0.5V a discontinuous surface layer was present (dark contrast in the figure), which was identified as a tribofilm [9]. This layer was not present under OCP conditions, although granulated wear debris was observed on the surface, which clearly had a lower average atomic number (as shown by the dark contrast in back scatter electron images). The wear surface from the cathodic condition exhibited evidence of a thin, intermittent, tribofilm.

3.2. Microstructural analysis and defect characterisation of subsurface

The deformed surface microstructure was investigated in detail to fully understand the microstructure that was being tested. Fig. 3 gives TEM bright field images of the worn surface under the different tested conditions. A tribofilm was found on all surfaces, but the extent depended strongly on the applied potential. For the anodic +0.5V condition, the worn surface was covered in a continuous tribofilm of varying thickness (30 nm to several hundred nm). This tribofilm has been investigated in detail, which is reported in Ref. [9], and generally had an amorphous structure. A continuous tribofilm was also observed for the OCP condition, but as with the anodic condition, the thickness varied

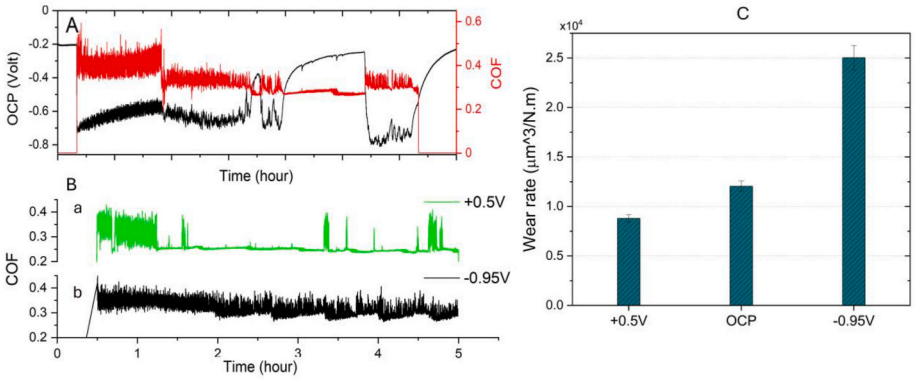

Fig. 1. Evolution of COF and OCP over time for A) OCP condition. B) COF evolution with time under applied potential +0.5V and −0.95V [9]. **[Printed with permission]**. C) Specific wear rates (in μm^3/Nm) for each test condition.

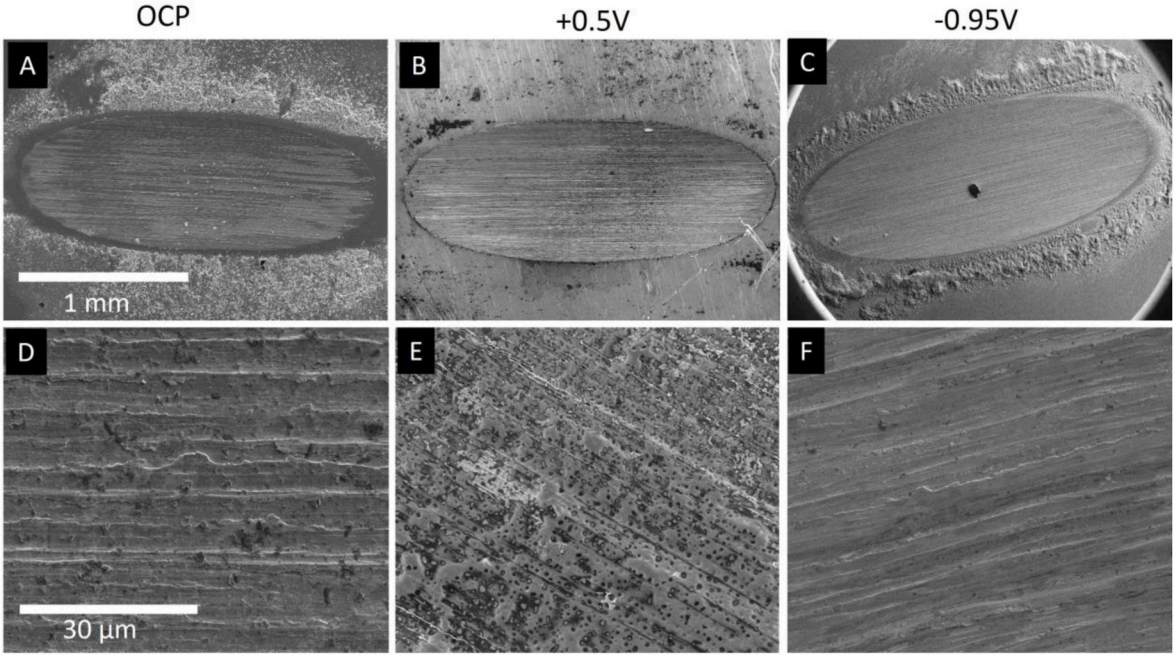

Fig. 2. SEM images of the worn surfaces under all three test conditions. D, E and F are the details taken from the centre of the wear tracks.

from place to place, with the thickest being of the order of 130 nm thick. The −0.95V sample again had a continuous uniform tribofilm, but with small dimensions of only 50–70 nm.

Below the tribofilm was a deformed layer, which is characteristic of worn surfaces. The extent of deformation varied with applied potential. In each case the outer deformed region comprised a nanocrystalline structure with lower strain layers below this. In order to quantify this, maps were taken using precession electron diffraction (PED) to determine the geometrically necessary dislocation (GND) density, Fig. 3J and K and L. The substructure in some regions was too fine to index. The dislocation density was far higher in the nanocrystalline regions compared to the coarser structures. In all cases, the dislocation density was higher in the α-phase than in the β-phase, which is expected given that the β-phase is softer than α-form. As expected, slip was primarily on the hcp basal planes, although prism slip was also observed in all cases. The GND density was highest in the +0.5V sample and the lowest with the −0.95V sample, with the OCP lying in between.

3.3. Mechanical properties of the tribo-surface

3.3.1. Nanoindentation results

Nanoindentation testing was carried out at a relative flat region close to one end of the wear-track, covering both worn and unworn surface. A very light polish was applied to expose the worn surface. A 10 × 20 array of indents with spacing of 10 μm in the x direction and 30 μm in the y direction was used to map local hardness variations. Fig. 4A shows such a map of the nanoindentation hardness results of the worn surface for the sample tested an anodic potential of +0.5V. It is clear that the wear process increased the hardness, but there is significant variation from point to point. The highest hardness appeared to coincide with the greater deformation, although the spatial resolution of the nanoindentation limits the ability to make this conclusion.

A cross section of the worn surface was undertaken. Two nanoindentation arrays, one just below and the other well below the wear induced deformation layer were carried out. The near-surface cross sectional array was obtained with a total 180 indents, while that well below the surface was a 9 × 9 array with 10 μm spacing in both x and y directions. The resulting nanoindentation hardness maps are presented in Fig. 4B. The hardness at the surface was up to 6.7 GPa, which then fell as a function of distance below the worn surface to that of the bulk of ~3.7 GPa.

3.3.2. Mechanical property test by micropillar compression

Hardness simply reflects the material's resistance to an indentation and is a relatively crude measure of the mechanical properties of the surface. To provide more detail, compression tests of micropillars were performed on the worn surfaces from all testing conditions to better understand the surface mechanical properties, particularly in the presence of a tribo-film.

Micropillar arrays were machined by FIB from the wear-track, with a pillar diameter of 1 μm (being slightly narrower at the top and wider at the bottom to give a conical shape) and a height to diameter aspect ratio of 3. The worn surface was much rougher than the unworn surface, however, the diameter of the top of the micropillar was small (1 μm) compared to the size of the grooves on wear tracks, and so relatively flat tops to the micropillar were obtained. Only areas without obvious wear debris were selected.

The micropillars were tested *in situ* by compression using a flat-punch diamond indenter inside the SEM chamber. Fig. 5A–D show a typical micropillar before and after the compression. A detail of the post-test micropillar, Fig. 6, shows slip steps in multiple directions on the surface along with a major shear band. Fig. 5E–G shows three stress-strain curves for each test condition, giving an indication of the variability from test to test. One of the curves for the anodic +0.5V condition shows continuous softening after yield. A cross section of the micropillar after testing indicated that this was a result of deformation concentrated in a single slip band, with no homogenous deformation, which can therefore be discounted.

Fig. 7 shows the stress-strain curves with the highest slope in the stress strain curve from Fig. 5 plotted together along with the stress strain curve for the unworn parent alloy. This was chosen on the basis that these micropillars will have exhibited the minimum of bending during the test. The micropillar stress-strain curves showed marked differences between the different test conditions. The OCP, −0.95V samples all showed an increase in yield stress compared to the unworn surface. However, low work hardening rates, and indeed work softening in all three cases meant the flow stress at failure was similar to the unworn surface. The micropillar cut from the +0.5V test exhibited

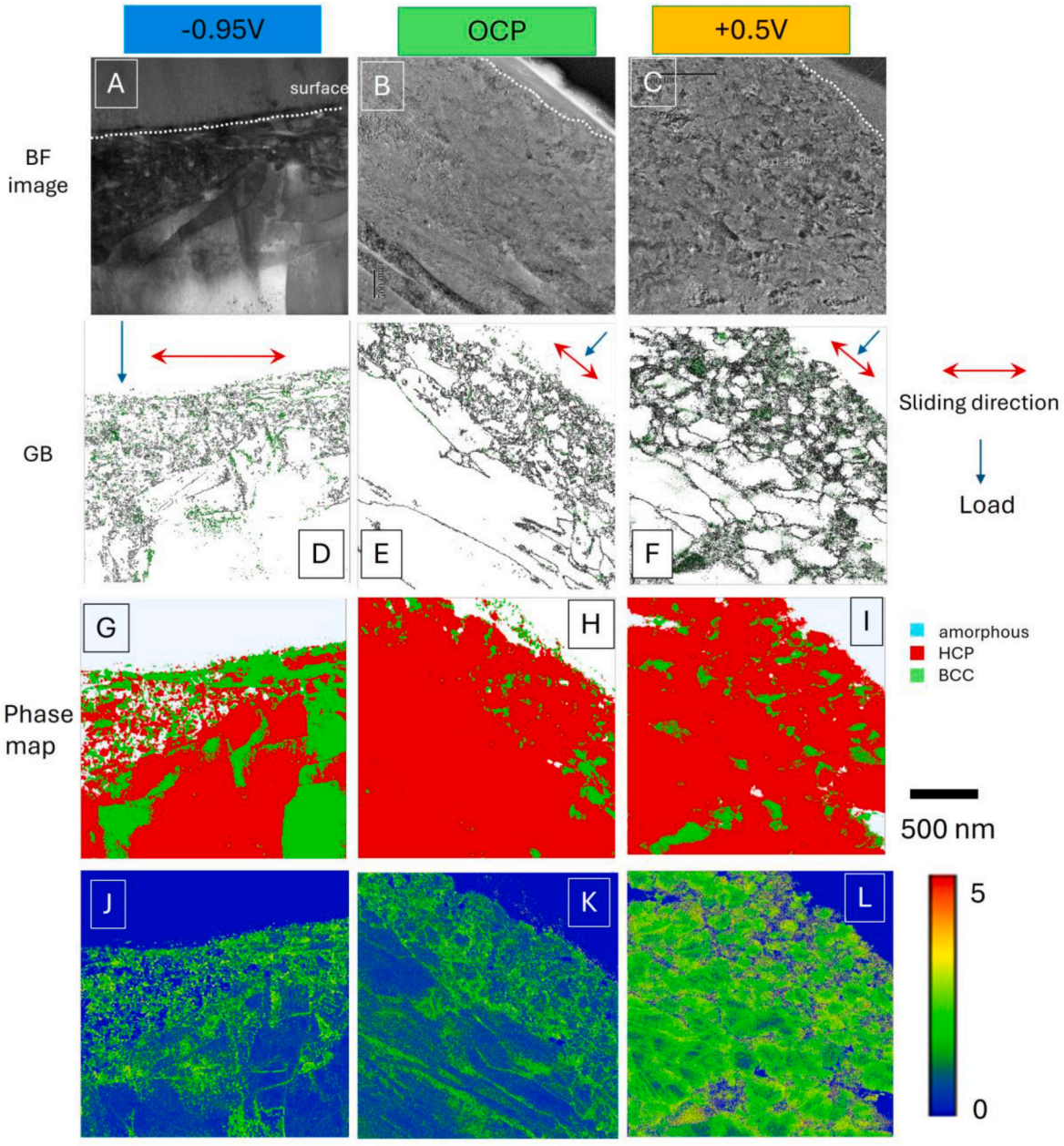

Fig. 3. FIB derived cross-sections of the worn surfaces. A, B and C are TEM bright field images showing the deformed surface structure for the three test conditions. The white dashed lines indicate the tribofilm. D, E and F are grain boundaries (GB) maps. G, H and I are phase maps where the hexagonal close-packed α-phase is red, and the body centre cubic β-phase is green. J, K and L are KAM maps. (red ←→ indicates the sliding direction and where the surface is located, and blue ↓ indicates the loading direction). The green colouration refers to the boundaries between 5 and 10°, and the back represents grain boundaries above 10°. (For interpretation of the references to colour in this figure legend, the reader is referred to the Web version of this article.)

substantially higher yield strength than all other tests with the flow stress at failure being ~2800 MPa, compared to the values of 1600–1800 MPa for all other test conditions.

To understand the deformation mechanisms within the micropillar during the compression tests, cross-sectional FIB specimens of the +0.5V and −0.95V samples were removed from the upper surface, axially into the pillars, and examined in the TEM. Fig. 8(A and B) give STEM dark field images of the +0.5V which show an outer region of high strain deformation of ~1 μm thick, with a much lower strain region below. The red arrows indicate slip/shear band steps on the surface of the pillar. Details of Fig. 8 are given in Fig. 9. The outer surface comprised a heavily deformed nanocrystalline layer approximately 1 μm thick. A sharp interface was observed between this nanocrystalline layer and the lower strain region below, in which individual dislocation lines could be imaged.

Fig. 10 gives TEM bright field and STEM annular dark field (ADF) images from the −0.95V test. Unfortunately, part of the upper (worn) surface of the pillar was lost during FIB preparation, with the black dotted line in Fig. 10 showing the true shape of the pillar. A substantial slip/shear band step had displaced the upper part of the pillar with respect to the lower part. Fig. 11 gives details of the sample in Fig. 10. The outer part (i.e. with the worn surface itself) showed evidence of deformation, Fig. 10A,B with a well-developed subgrain structure, Fig. 10C. The sharp interface between the outer part and the lower strain region below is shown in Fig. 10D. The interface appears to be a single slip plane that accommodated very high strain.

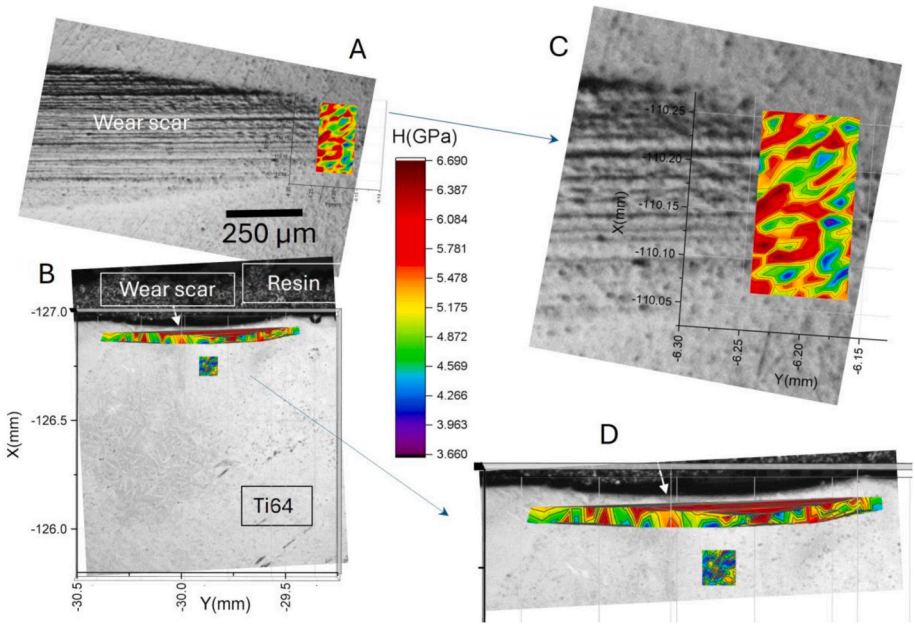

Fig. 4. Hardness test on A) wear scar and B) subsurface under the worn surface of +0.5V sample. Both show the hardness increased as a result of frictional contact. C) and D) are the enlarged hardness maps superimposed on the SEM images for the tested regions.

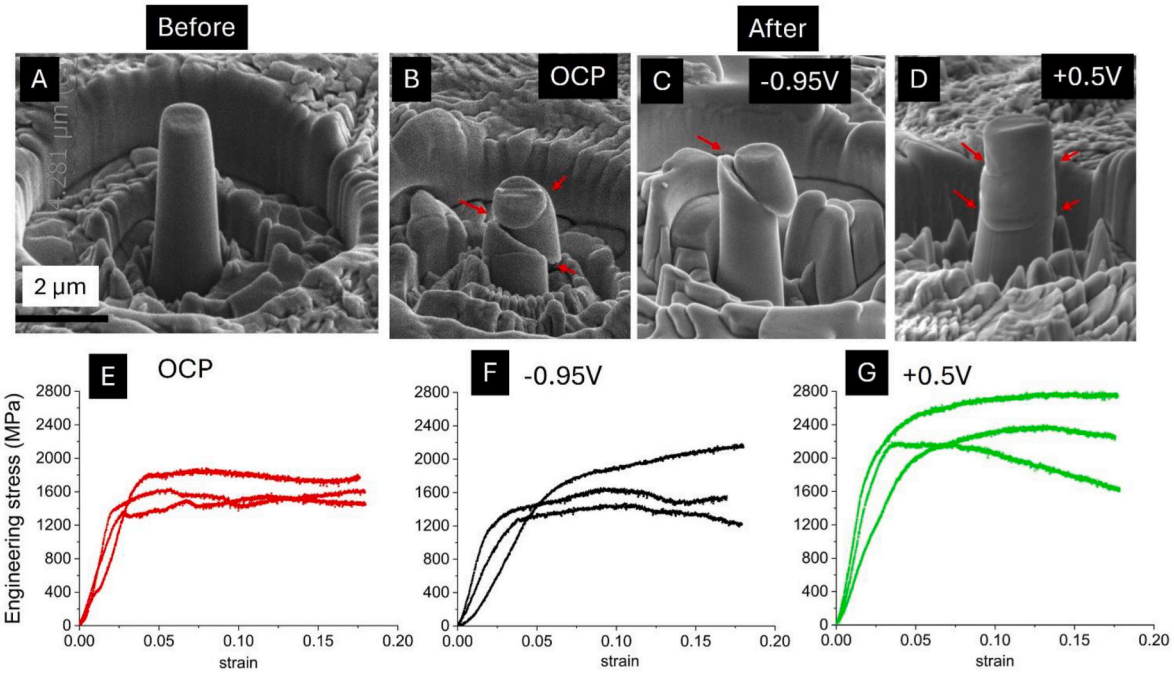

Fig. 5. *In situ* micropillar compression on the worn surfaces from various test conditions. Represent images for pillars A) before compression; B) OCP after compression, C) −0.95V after compression and D) +0.5V after compression. The stress-strain curves for the E) OCP, F) −0.95V, and G) +0.5V. Red arrows indicate bending/slip. (For interpretation of the references to colour in this figure legend, the reader is referred to the Web version of this article.)

4. Discussion

4.1. Tribocorrosion induced surface microstructural changes

The tribocorrosion wear behaviour of Ti-6Al-4V as a function of applied potential has been studied in detail and is presented in Ref. [9]. The current tests were made under the same conditions as presented in Ref. [9], and so the detailed friction and wear will not be discussed. Of note, the lowest specific wear rate was found for the anodic +0.5V condition, Fig. 1, with the highest specific wear rate observed for the cathodic −0.95V condition. This has been explained by the extent of a surface tribofilm present (of highly complex structure), which was most extensive under anodic conditions and least extensive under cathodic conditions [9].

The applied potential had a strong effect on the friction induced surface structures, in terms of depth of deformation, extent of surface strain, and the phase constitution (in addition to the tribofilm mentioned above). Fig. 3 gives TEM bright field images of FIB cross-sections of the worn surface, along with the grain boundary distribution, the geometrically necessary dislocation (GND) distribution and the phase

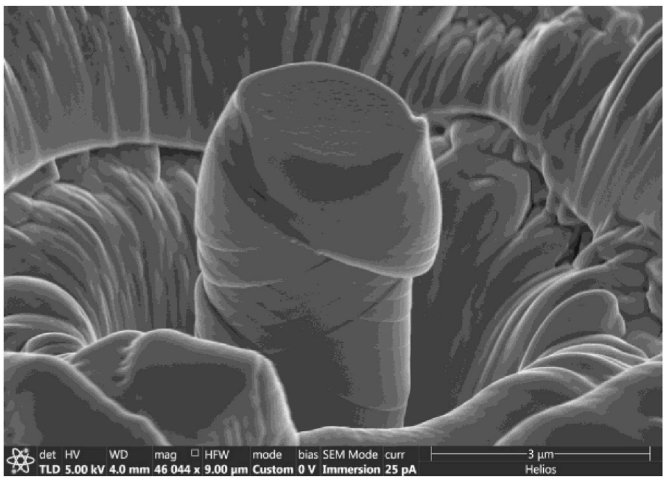

Fig. 6. Detail of a micropillar from the OCP test after compression, showing slip bands on the surface and a major shear band.

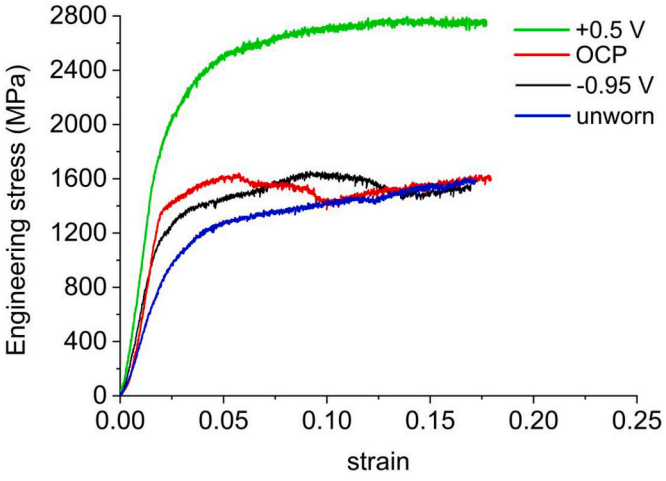

Fig. 7. A comparison of the stress-strain curves for the 3 test conditions, taking the curves with the steepest slope, with the unworn surface.

distribution. The −0.95V and the OCP samples were broadly similar, with a poorly developed nanocrystalline structure at the surface, which contained a high density of GNDs. There was then a relatively sharp interface to a lower strain region, which contained subgrain structures and other classic deformation substructures. Interestingly, the −0.95V sample contained a higher than expected proportion of β-Ti, which was not seen in the other samples. This was presumably just reflecting the natural variation in β-Ti throughout the sample.

The +0.5V sample was markedly different to the −0.95V and OCP samples. The nanocrystalline layer was far more developed, containing a finer structure, a higher GND density and extending to further below the worn surface (~1 µm), Fig. 3. The observation that anodic conditions produce greater surface strain compared to OCP or cathodic conditions has been made on several occasions. For example, a detailed correlation between surface oxide and depth of deformation was made for CoCrMo alloys by Qi et al. [10], and for 304L stainless steel by Perret et al. [13], Favero et al. [26] and Bidiville et al. [27]. The surface oxide promoted by the anodic conditions is believed to block the annihilation of dislocations at the surface (which occurs under cathodic conditions in the absence of an oxide) leading to greater surface strain accumulation. However, the correlation between the formation of a well-developed nanocrystalline structure and the wear rate has not been established. For example, in the work of Perret et al. [13] the formation of a thick nanocrystalline layer coincided with the highest wear rate, while Namus et al. [12] showed that there was very little correlation of wear rates and material grains size from nanocrystalline through to conventional micron grain size for CoCrMo alloys.

4.2. Mechanical properties of the surface structures

There were differences in the observed mechanical properties between the nanohardness results and those obtained from the micropillars, compare Fig. 4 with Figs. 6 and 7. For the +0.5V test, the UTS measured by the micropillar test of ~2.8 GPa corresponds to a hardness of ~9.2 GPa, which is considerably higher than the maximum values measured of ~6.7Ga. This contrasts Battaile et al. [11], who found that the nanoindendation of a worn single crystal nickel, containing a tribofilm, was about twice the value found from micropillar experiments. However, care should be taken in comparing the two techniques of nanoindentation and micro/nanopillars as there are several important differences: the two techniques sample different volumes, both techniques show significant size effects and each technique has inherent errors.

Many nanoindentation experiments have shown an inverse relationship between the hardness and the indentation depth [16–22]. With nanoindentation the plastic deformation is confined within a small volume and non-uniform stresses and strains occur around the indent. In other words, strong strain gradients are promoted around the indent, which is believed to be the origin of this indentation size effect (ISE) [28]. Moreover, when making nanoindentation measurements on a worn surface, the surface roughness will introduce errors, which will become greater the closer the indentation size is to the scale of the roughness. In the current work, care was taken to choose flat regions, but nevertheless and error is inevitable.

It is not only nanoindentation that shows a size effect, but the mechanical properties measured from micro/nanopillar experiments also show a distinct dependence on the size of the pillar [28]. For example, Uchic et al. [29] observed an increase in the flow stress from 250 MPa for a 20 mm diameter pillar to 2 GPa for a 0.5 mm diameter pillar for the same material in the same prior condition. These flow stresses are also much higher than observed in the bulk material, showing the size effect associated with testing pillars. Similar observations have been seen by Refs. [28,29]. The precise mechanisms that lead to the size effect are beyond the scope of the current discussion, but the essence is that the increase in strength is associated with the reduction in the availability of dislocation sources ("single arm sources [30]" or nucleation from the free surface [31]) as the pillar size is reduced, with the ultimate condition where dislocations are only nucleated from the free surface in very small pillars (of an exact size depending on the material). It is clear that a straight comparison of nanoindentation hardness and micropillar derived mechanical properties should not be made unless the size effect of both techniques is fully understood for the material in question.

When interpreting the mechanical properties derived from the micropillars it is important to consider the effect of the micropillar geometry on the mechanical properties measured. Zhang et al. undertook a mechanics analysis of the effect of the taper and eccentricity of the micropillar on the measured mechanical properties [32]. They found that the measured UTS was overestimated by 10 % for a 1° taper rising to 20 % for a 3° taper, although they did not offer experimental validation of the mechanics analysis. This, in itself suggests that the difference between micropillar and hardness results found here is less than the experimentally recorded values.

There are several further factors which should be considered when interpreting micropillar results, namely the volume of the worn surface sampled, the effect of prior deformation structures on the deformation mechanisms and the observed deformation mechanisms. Before considering the mechanical properties and the volumes tested it is important to consider the known knowledge on the effect of prior straining a pillar on the observed mechanical properties. If a pillar is pre-

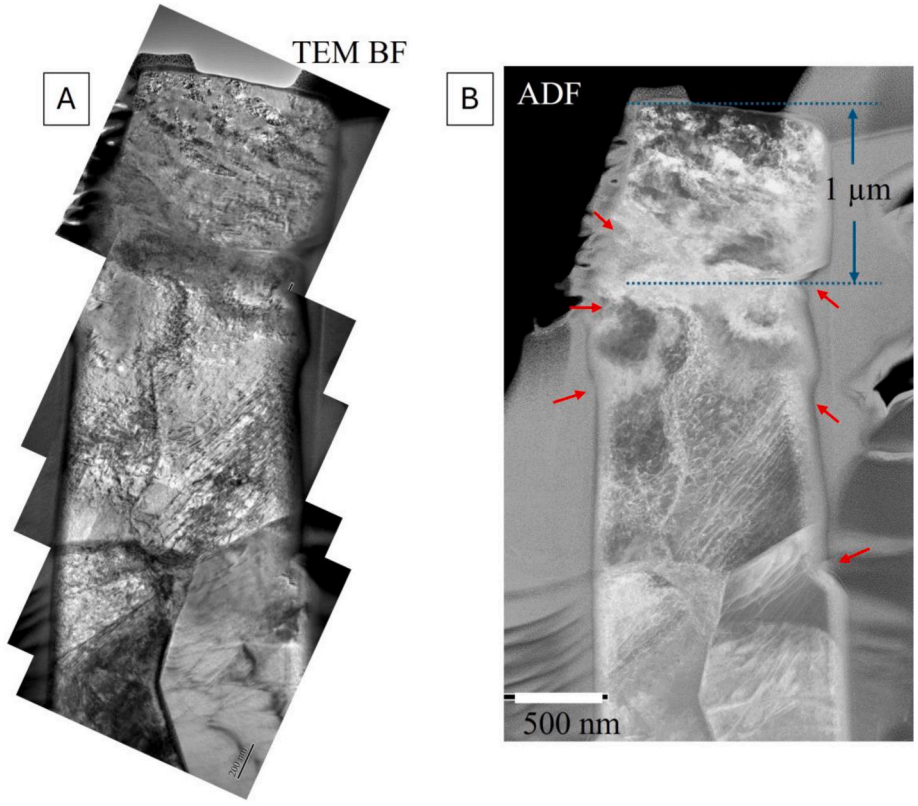

Fig. 8. Cross-sectional (A) bright field TEM image and (B) STEM annular dark field (ADF) image for the +0.5V sample after micropillar compression. The red arrows indicate the slip/shear band steps on the surface of both pillars. The upper ~1 μm is a heavily deformed nanocrystalline region, with a lower strain region below this. (For interpretation of the references to colour in this figure legend, the reader is referred to the Web version of this article.)

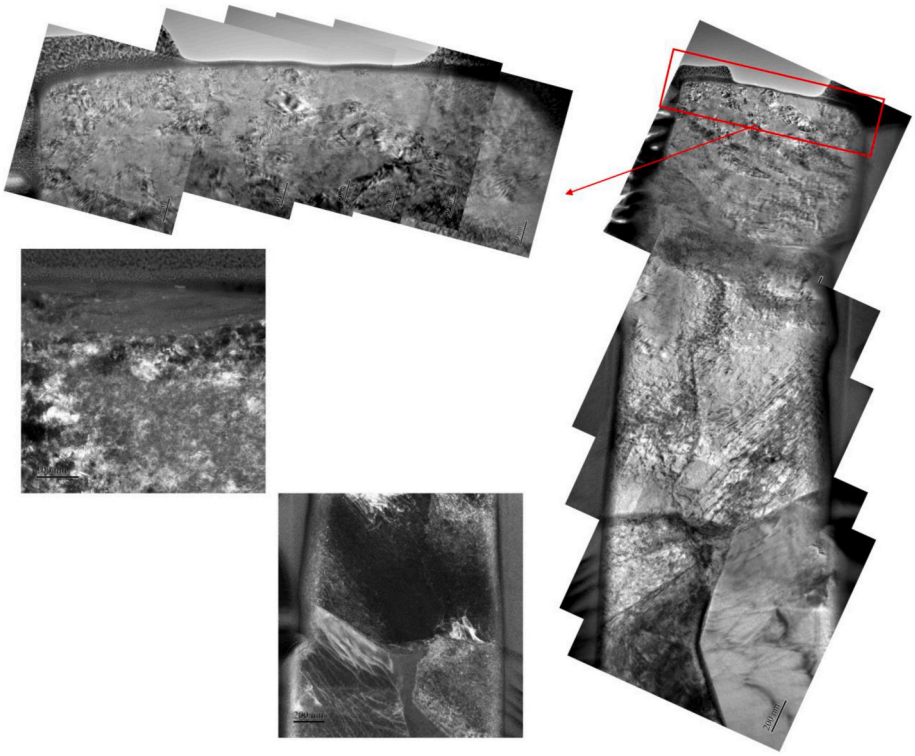

Fig. 9. TEM images of the micropillar shown in Fig. 8A and B after micropillar compression from the +0.5V test. The right-hand image shows the pillar as a whole. The top left image shows a TEM bright field image of the original worn surface, while the image below is a STEM annular dark field (ADF) image of the worn surface showing the nanocrystalline state. The lower middle image is an annular dark field STEM image showing the dislocation structures in the region below the nanocrystalline structure.

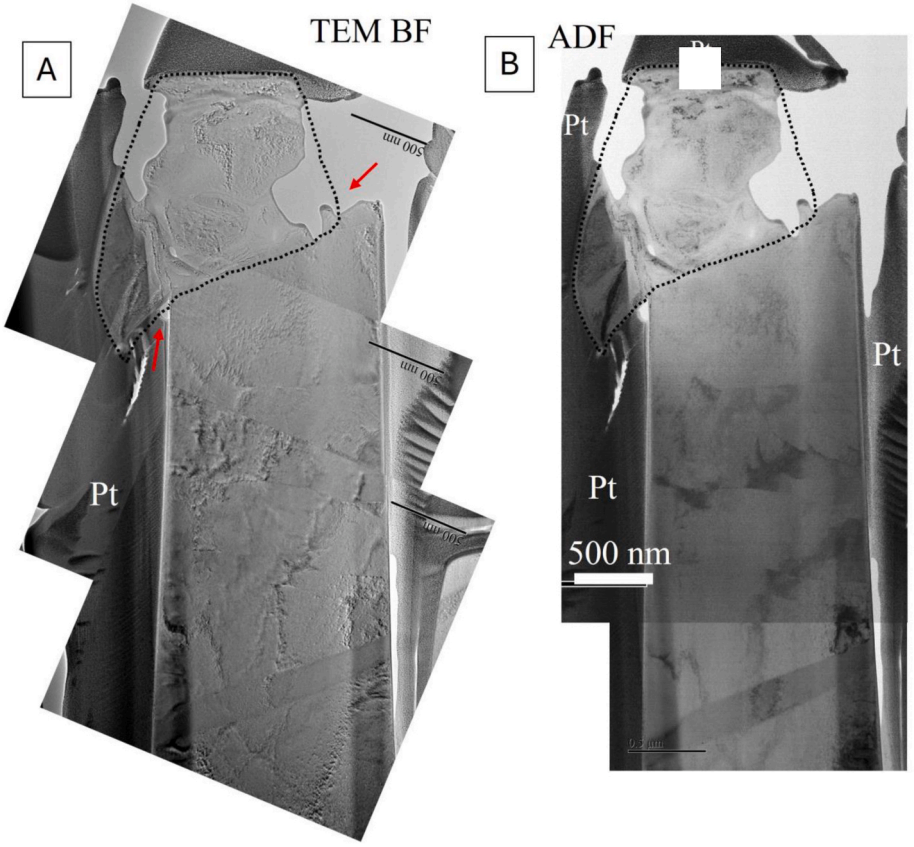

Fig. 10. Cross-sectional (A) bright field TEM image and (B) STEM annular dark field (ADF) image for the −0.95V sample after micropillar compression. The red arrows indicate a slip/shear band step on the surface of the pillar. (For interpretation of the references to colour in this figure legend, the reader is referred to the Web version of this article.)

deformed to increase its dislocation density, then on subsequent testing the pillar is found to be softer than the same material tested without prestraining [11,33,34]. This is the opposite behaviour that would be found in a macroscopic tensile or compression test. It is well known that dislocations can lead to either strengthening or weakening of a crystal. In a conventional bulk test, the increase in dislocation density with strain leads to a greater number of elastic interactions, which makes dislocation motion more difficult and therefore higher stresses are required to move dislocations, resulting in Taylor hardening. In contrast, in the small volume of a pillar with a prior existing dislocation structure, the motion of these existing dislocations over small slip lengths results a yield drop [34]. Therefore, the interpretation of the stress strain curves in Figs. 6 and 7 should consider these observations of prior strained pillar tests.

Despite the small size of the pillars and the small number of grains contained within the diameter, the presence of multiple slip steps, with at least two slip systems, on the surface of the micropillar, e.g. Fig. 6, suggests conventional dislocation slip plasticity, with no evidence of alternative deformation modes such as twinning or grain boundary sliding. The presence of slip steps on the surface of all micropillars, up to the worn surface, does indeed show that the tests sampled the entire worn surface volume. However, the majority of the micropillars failed by localisation of slip into a confined shear zone, in which significant strain was accommodated (see Figs. 5 and 6 and the displacement in the TEM image in Fig. 10). Battaile et al. [11] also observed that for single crystal Ni 250 nm diameter pillars, the unworn pillar deformed homogeneously, with multiple slip steps evenly distributed across the pillar, while a pillar of the same dimensions removed from a worn surface deformed by slip localisation in a shear band. They attributed this to "locally weak hot spots" [11] where, because of the limited slip systems available (partly because of the small deformation volume), strain localisation occurs, either from easy slip activation on that plane, or because the resolved shear stress on other slip systems is too low to activate slip on them, or both.

Clearly, the depth of deformation sampled differed between the samples, but of course this is what the experiments were intended to probe. The micropillar test will have sampled a deformation structure that varies with depth in the pillar. While there were differences in the tribolayer on the surface as a function of the test potential, it is unlikely that this would have contributed to the mechanical properties observed. There is a dead zone immediately below the punch (through which the load is applied) and so, provided the tribolayer does not reduce the friction between punch and pillar to <0.1 (which induces buckling of the pillar [35], which was not seen here), the presence of the tribolayer will not affect the mechanical properties.

There was significant variability in the stress strain curves obtained from the micropillars, as shown in Fig. 5. This is to be expected when sampling small volumes of a very heterogeneous structure. For the OCP test, the flow curves followed a similar trend of undulating flow behaviour whereby periods of work hardening were followed by work softening. This work hardening/work softening behaviour has been seen before when testing worn surfaces as shown by Stoyanov et al. [24] for tungsten, although they do not comment on the reasons for the shape of the flow curve, and by Battaile et al. [11] for nickel. Battaile et al. suggest that the work hardening is a result of homogeneous slip events, while the work softening is associated with the strain localisation. This is consistent with the current work. Indeed, videos of the micropillar deformation (see additional material) showed that the work softening coincided with the formation of strain localisation across the specimen, which are clearly seen in, for example, Figs. 5B and 6.

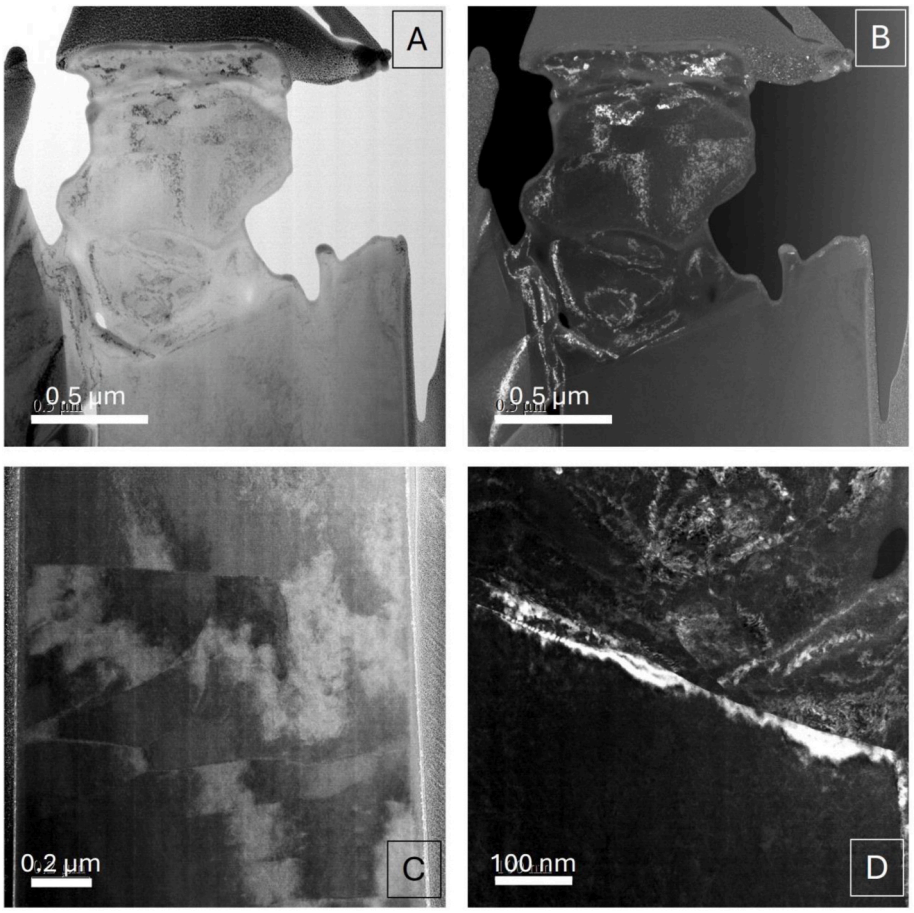

Fig. 11. TEM images showing details of the micropillar shown in Fig. 10 after micropillar compression from the −0.95V test. (A, B) ADF STEM and high angle annular dark field (HAADF) STEM images of the top of the micropillar (with worn surface at the top), showing an interface between heavily deformed material and a low strain region. (C) ADF STEM image showing well developed subgrain structure from the upper region of (A,B). (D) HAADF STEM image of the sharp interface between high strain (upper) and low strain (lower) regions.

The behaviour of the −0.95V sample, Fig. 5F, was similar to that of the OCP test, with similar flow stress values, although one curve in Fig. 5F showed continued hardening up to failure. The appearance of the micropillars after the testing were similar, with limited slip steps and evidence of shear localisation, which ultimately led to failure. The worn surface microstructure shown in Fig. 3 was broadly similar between the −0.95V and OCP conditions, with similar depths of deformation and similar densities of geometrically necessary dislocations. Therefore, it is perhaps not surprising that the measured mechanical properties of the worn surfaces are similar.

The flow stress at failure was similar for the −0.95V and OCP conditions, but also the same as for the unworn surface, Fig. 7. The unworn surface exhibited a lower yield strength than these two conditions, but exhibited homogeneous work hardening up to failure, without evidence of strain localisation. This is consistent with the literature that the strain localisation occurs as a result of the prior deformed structure (from wear), which limits homogeneous deformation [11,24]. The strain localisation event could clearly be seen in the TEM images of the FIB sections after the test in Figs. 10 and 11. Indeed, Fig. 11 D shows how narrow the slip localisation event is. Strain localisation results in softening, such that the even with such a heavily deformed worn surface structure, the flow stress is still no higher than the undeformed state. This factor clearly limits the ability of micropillars to accurately measure the mechanical properties of wear induced deformed structures.

The +0.5V test showed quite different behaviour to the other tests, Fig. 5G. In one case, a major shear localisation occurred at yielding which resulted in work softening up to failure. However, in the other two tests work hardening was observed nearly to the point of failure, and the flow stresses were significantly (400–1000 MPa) higher than all other tests. Examination of the micropillars during and after the tests showed that deformation was more homogeneous and that strain localisation events were fewer and less well developed. The TEM results post investigation, Figs. 8 and 9, is consistent with this, showing evidence of homogeneous slip. The absence of strain localisation in the nanocrystalline structure suggests that the ultra-fine, randomly oriented, grains are good at resisting such localised shear events. In this case, it would appear that the micropillar test was better at measuring the mechanical properties of the nanocrystalline surface, although it should be remembered that the stress system will be different in the micropillar test compared to a contact asperity. As such, there remains no test that truly tests the mechanical properties of a worn surface, but the micropillar tests can be regarded as complementary to the nano-indentation hardness.

5. Conclusions

1. Tribocorrosion tests at −0.95V, OCP and +0.5V conditions showed differences in wear rate, with the −0.95V showing the highest wear rate and the +0.5V exhibiting the lowest wear rate. The extent of friction induced surface deformation was similar for the −0.95V and OCP tests, showing a poorly developed, relatively thin, nanocrystalline layer with a subgrain structure below this. In contrast, the +0.5V exhibited a well-developed (~1 μm) nanocrystalline layer,

which was believed to be promoted by the surface oxide that prevents dislocation annihilation.
2. Little correlation was observed between the nanoindentation hardness and micropillar derived mechanical properties for the +0.5V sample. The two techniques sample different volumes, but also the slip behaviour within the volume sampled is different. Both techniques show a strong size effect, which must be understood before comparisons can be made.
3. The compression tests of micropillars removed from an unworn surface exhibited sustained work hardening up to failure with homogeneous dislocation slip being found in the specimen.
4. The compression tests of micropillars removed from the −0.95V and OCP wear tests exhibited work hardening followed by immediate work softening, such that the flow stress at failure was the same as that observed for the unworn surface. The work softening is associated with strain localisation (shear bands), where high strains are accommodated in a narrow band. This work softening prevented this high strain prior structure being any stronger than the unworn surface, bringing into question the validity of using micropillars to test the mechanical properties of this type of surface.
5. The stress strain curve from the +0.5V micropillar test exhibited more homogeneous work hardening giving much higher flow stress values than the tests at −0.95V and OCP. TEM suggested that this was associated with the nanocrystalline layer preventing strain localisation. Therefore, in this case the micropillar compression tests gave a better indication of the mechanical properties of the nanocrystalline layer.
6. The micropillar and nanoindentation give different information about the surface mechanical properties that can be regarded as complementary.

Author contributions

JQ: conceptualize the idea, designed and conducted the experiments, wrote the original draft. WMR: Supervision, validation, writing - review & editing. BJI contributed discussion, paper review & editing. JN: contributed the PET data collecting and processing and discussion. MB: contributed the micropillar compression data collecting, processing and discussion. All authors reviewed the manuscript.

Declaration of competing interest

The authors declare the following financial interests/personal relationships which may be considered as potential competing interests: None.

Acknowledgement

This work is supported by the Engineering and Physical Sciences Research Council (grant number EP/001766/1) as a part of 'Friction: The Tribology Enigma' Programme Grant (www.friction.org.uk), a collaboration between the Universities of Leeds and Sheffield.

The authors wish to acknowledge the Henry Royce Institute for Advanced Materials, funded through EPSRC grants EP/R00661X/1, EP/S019367/1, EP/P02470X/1 and EP/P025285/1, for JEOL JEM-F200 access at Royce@Sheffield.

Appendix A. Supplementary data

Supplementary data to this article can be found online at https://doi.org/10.1016/j.wear.2025.205785.

References

[1] V. Swaminathan, J.L. Gilbert, Fretting corrosion of CoCrMo and Ti6Al4V interfaces, Biomaterials 33 (22) (2012) 5487–5503, https://doi.org/10.1016/j.biomaterials.2012.04.015.
[2] M.T. Mathew, J.J. Jacobs, M.A. Wimmer, Wear-corrosion synergism in a CoCrMo hip bearing alloy is influenced by proteins, Clin. Orthop. Relat. Res. 470 (11) (Nov. 2012) 3109–3117, https://doi.org/10.1007/s11999-012-2563-5.
[3] W.M. Rainforth, P. Zeng, L. Ma, A.N. Valdez, T. Stewart, Dynamic surface microstructural changes during tribological contact that determine the wear behaviour of hip prostheses: metals and ceramics, Faraday Discuss 156 (2012) 41, https://doi.org/10.1039/c2fd00002d.
[4] W.M. Rainforth, J. Nutting, R. Stevens, Deformation structure induced by sliding contact, Philos. Mag. 66 (4) (1992) 621–641.
[5] I. Ghamarian, P. Samimi, Y. Liu, B. Poorganji, V.K. Vasudevan, P.C. Collins, Characterizing the nano-structure and defect structure of nano-scaled non-ferrous structural alloys, Mater. Char. 113 (2016) 222–231, https://doi.org/10.1016/j.matchar.2015.10.002.
[6] X. Liu, Y. Zhou, X. Zhu, D. Wang, Q. Fan, The failure mechanism at adiabatic shear bands of titanium alloy: high-precision survey using precession electron diffraction and geometrically necessary dislocation density calculation, Mater. Sci. Eng. A 746 (Feb. 2019) 322–331, https://doi.org/10.1016/j.msea.2019.01.016.
[7] I. Ghamarian, Y. Liu, P. Samimi, P.C. Collins, Development and application of a novel precession electron diffraction technique to quantify and map deformation structures in highly deformed materials—as applied to ultrafine-grained titanium, Acta Mater. 79 (August) (Oct. 2014) 203–215, https://doi.org/10.1016/j.actamat.2014.06.063.
[8] I. Ghamarian, P. Samimi, A. Telang, V.K. Vasudevan, P.C. Collins, Characterization of the near-surface nanocrystalline microstructure of ultrasonically treated Ti-6Al-4V using ASTAR^{TM}/precession electron diffraction technique, Mater. Sci. Eng. A 688 (November 2016) (2017) 524–531, https://doi.org/10.1016/j.msea.2017.02.029.
[9] J. Qi, D. Guan, J. Nutter, B. Wang, W.M. Rainforth, Insights into tribofilm formation on Ti-6V-4Al in a bioactive environment: correlation between surface modification and micro-mechanical properties, Acta Biomater. 141 (2022) 466–480, https://doi.org/10.1016/j.actbio.2022.01.027.
[10] J. Qi, L. Ma, P. Gong, W.M. Rainforth, Investigation of the wear transition in CoCrMo alloys after heat treatment to produce an HCP structure, Wear 518 (2023) 204649, https://doi.org/10.1016/j.wear.2023.204649.
[11] C.C. Battaile, B.L. Boyce, C.R. Weinberger, S.V. Prasad, J.R. Michael, B.G. Clark, The hardness and strength of metal tribofilms: an apparent contradiction between nanoindentation and pillar compression, Acta Mater. 60 (4) (2012) 1712–1720, https://doi.org/10.1016/j.actamat.2011.11.059.
[12] R. Namus, P. Zeng, W.M. Rainforth, Correlation of the wear transition in CoCrMo alloys with the formation of a nanocrystalline surface layer and a proteinaceous surface film, Wear 376 (377) (2017) 223–231, https://doi.org/10.1016/j.wear.2016.11.046.
[13] J. Perret E. Boehm-Courjault, M. Cantoni, S. Mischler, A. Beaudouin, W. Chitty, J.-P. Vernot, EBSD, SEM and FIB characterisation of subsurface deformation during tribocorrosion of stainless steel in sulphuric acid, Wear 269 (2010) 383–393, https://doi.org/10.1016/j.wear.2010.04.023.
[14] S.G. Maldonado, S. Mischler, M. Cantoni, W.J. Chitty, C. Falcand, D. Hertz, Mechanical and chemical mechanisms in the tribocorrosion of a Stellite type alloy, Wear 308 (1–2) (2013) 213–221, https://doi.org/10.1016/j.wear.2013.04.007.
[15] R. Namus, W.M. Rainforth, Y. Huang, T.G. Langdon, Effect of grain size and crystallographic structure on the corrosion and tribocorrosion behaviour of a CoCrMo biomedical grade alloy in simulated body fluid, Wear 478–479 (2020) 203884, https://doi.org/10.1016/j.wear.2021.203884.
[16] N.A. Stelmashenko, M.G. Walls, L.M. Brown, Y.V. Millman, Microindentations on W and Mo oriented single crystals: an STM study, Acta Metall. Mater. 41 (1993) 2855–2865.
[17] M.S. De Guzman, G. Neubauer, P. Flinn, W.D. Nix, The role of indentation depth on the measured hardness of materials, Mater. Res. Symp. Proc. 308 (1993) 613.
[18] M. Atkinson, Further analysis of the size effect in indentation hardness tests of some metals, J. Mater. Res. 10 (1995) 2908–2915, https://doi.org/10.1557/JMR.1995.2908.
[19] Q. Ma, D.R. Clarke, Size dependent hardness of silver single crystals, J. Mater. Res. 10 (1995) 853.
[20] W.J. Poole, M.F. Ashby, N.A. Fleck, Micro-hardness of annealed and work-hardened copper polycrystals, Scripta Metall. Mater. 34 (1996) 559–564.
[21] K.W. McElhaney, J.J. Vlassak, W.D. Nix, Determination of indente tip geometry and indentation contact area for depth-sensing indentation experiments, J. Mater. Res. 13 (1998) 1300.
[22] S. Suresh, T.G. Nieh, B.W. Choi, Nano-indentation of copper thin films on silicon substrates, Scripta Mater. 41 (1999) 951–957, https://doi.org/10.1016/S1359-6462(99)00245-6.
[23] R.R. Chromik, Y. Zhang, Nanomechanical testing of third bodies, Curr. Opin. Solid State Mater. Sci. 22 (4) (Aug. 2018) 142–155, https://doi.org/10.1016/j.cossms.2018.05.001.
[24] P. Stoyanov R. Merz, P.A. Romero, F.C. Wahlisch, O. Torrents, R. Gralla, P. Stemmer, M. Kopnarski, M. Moseler, R. Bennewitz, M. Dienwiebe, Surface softening in metal–ceramic sliding contacts: an experimental and numerical investigation, ACS Nano 9 (2) (Feb. 2015) 1478–1491, https://doi.org/10.1021/nn505968m.

[25] G.M. Pharr, An improved technique for determining hardness and elastic modulus using load and displacement sensing indentation experiments, J. Mater. Res. 7 (6) (Jun. 1992) 1564–1583, https://doi.org/10.1557/JMR.1992.1564.
[26] M. Favero, P. Stadelmann, S. Mischler, Effect of the applied potential of the near surface microstructure of a 316L steel submitted to tribocorrosion in sulfuric acid, J. Phys. D Appl. Phys. 39 (2006) 3175–3183.
[27] A. Bidiville, M. Favero, P. Stadelmann, S. Mischler, Effect of surface chemistry on the mechanical response of metals in sliding tribocorrosion systems, Wear 263 (2007) 207–217.
[28] J.R. Greer, W.C. Oliver, W.D. Nix, Size dependence of mechanical properties of gold at the micron scale in the absence of strain gradients, Acta Mater. 53 (2005) 1821–1830, https://doi.org/10.1016/j.actamat.2004.12.031.
[29] M.D. Uchic, D.M. Dimiduk, J.N. Florando, W.D. Nix, Sample dimensions influence strength and crystal plasticity, Science 305 (2004) 986–989, https://doi.org/10.1126/science.1098993.
[30] C.R. Weinberger, W. Cai, The stability of Lomer-Cottrell jogs in nanopillars, Scripta Mater. 64 (2011) 529–532, https://doi.org/10.1016/j.scriptamat.2010.11.037.
[31] T.A. Parthasarathy, S.I. Rao, D.M. Dimiduk, M.D. Uchic, D.R. Trinkle, Contribution to size effect of yield strength from the stochastics of dislocation source lengths in finite samples, Scripta Mater. 56 (2007) 313–316, https://doi.org/10.1016/j.scriptamat.2006.09.016.
[32] W. Zhang, Z. Ma, H. Zhao, L. Ren, A calibration method of micropillar compression testing for taper and eccentricity induced errors, IEEE Trans. Instrum. Meas. 70 (2021) 6010006, https://doi.org/10.1109/TIM.2021.3107042.
[33] H. Bei, S. Shim, G. Pharr, E. George, Smaller is stronger: the effect of strain hardening, Acta Mater. 56 (2009) 4762–4770, https://doi.org/10.1016/j.actamat.2009.08.024.
[34] S. Lee, S. Han, W. Nix, Uniaxial compression of fcc Au nanopillars on an MgO substrate: the effects of prestraining and annealing, Acta Mater. 57 (2009) 4404–4415, https://doi.org/10.1016/j.actamat.2009.06.002.
[35] D. Raabe, D. Ma, F. Roters, Effects of initial orientation, sample geometry and friction on anisotropy and crystallographic orientation changes in single crystal microcompression deformation: a crystal plasticity finite element study, Acta Mater. 55 (2007) 4567–4583.